International Journal of Heat and Mass Transfer 89 (2015) 996–1006

Contents lists available at ScienceDirect

International Journal of Heat and Mass Transfer

journal homepage: www.elsevier.com/locate/ijhmt

On discriminating sizes of CFD generated bubbles with signal processing analysis

Muhammad Salman Khan [a], Gonzalo Montes [b], Alvaro Valencia [c,*], Sohail Masood Bhatti [a], Nestor Becerra Yoma [a]

[a] Department of Electrical Engineering, Universidad de Chile, Santiago, Chile
[b] Department of Mining Engineering, Universidad de Chile, Santiago, Chile
[c] Department of Mechanical Engineering, Universidad de Chile, Santiago, Chile

ARTICLE INFO

Article history:
Received 27 January 2015
Received in revised form 2 June 2015
Accepted 3 June 2015
Available online 18 June 2015

Keywords:
Bubble size classification
Computational fluid dynamics
Signal processing
Short-term Fourier analysis
Pattern recognition

ABSTRACT

The aim of this research work is to propose a signal processing based technique to classify and estimate bubble sizes. Bubbles are generated by computational fluid dynamics simulations. Local measuring points for velocity and pressure are set, and the captured data are analyzed using signal processing. The signal analysis includes the generation of templates for signal measurements of different bubble sizes using the short-time Fourier transform. Euclidean distances between templates of the different bubble size classes are subsequently computed. An inter/intra-class distance based matrix methodology is proposed to assess the discriminability of the Fourier-based template representation. The results indicate that the proposed technique based on signal processing can lead to the discrimination of bubble sizes with the information of bubbles passing through a single sensor point. Moreover, the model presented in this paper suggests that the analysis window size may play a highly important role in the discriminability according to the range of target bubble sizes.

1. Introduction

Heterogeneous systems are found in industrial operations, such as mineral processing, surfactant industries, food processing plants, the pulp and paper industry, pharmaceutical applications, and petrochemicals, among others [1]. The purpose of implementing these systems ranges from conducting heterogeneous reactions to achieving difficult separation operations. To understand the performance of processes where heterogeneous systems are in use requires achieving a correct and comprehensive description of this environment. Studies have contributed to identifying the main factors and variables affecting the performance of different heterogeneous processes; however, difficulties in assessing the variables in real systems are still found [2]. As a consequence of the latter, many efforts have been put into developing new and improved methodologies to obtain robust and accurate measurements of these variables. Two- and three-phase bubble flows are not an exception of this, particularly when the bubble size and also the gas hold-up impacts the bubble velocity [3,4]. Many heterogeneous reactions occur in these types of environments such as fluidized bed reactions, froth flotation, and leaching reactions [5]. Sizing gas bubbles could be useful in some mining processes, such as the froth flotation process- a selective separation process used to extract valuable minerals from raw ore, such as copper, gold and zinc [6]. The minerals are made hydrophobic to attach to the air bubbles that are continuously pumped into the tank [7]. Some of the most relevant parameters to be assessed in these systems are the bubble size, bubble velocity, bubble terminal velocity and gas hold-up. Because many of these processes usually take place under churn turbulent conditions, these features are difficult to evaluate and predict [8]. The aim of this scientific contribution is to develop a proxy based on signal processing to identify bubbles and to extract information, namely, bubble size distribution, from a bubbly flow created using computational fluid dynamics.

The applicability of the signal processing based method proposed in this paper covers a wide range of industrial fields [9]. It can be applied to mineral froth flotation where bubbles carrying economically valuable particles move across a pulp phase by defining the rate at which particles enter the froth phase that is crucial for understanding froth drop back mechanisms and the overall efficiency of the process. Both of the mentioned outcomes are directly related to the bubble size [10]. Furthermore, the applicability of the proposed technique also covers many gas–liquid multiphase reactions that are relevant for refineries and petrochemical industries where bubble size defines the rate at

* Corresponding author.
E-mail address: alvalenc@ing.uchile.cl (A. Valencia).

http://dx.doi.org/10.1016/j.ijheatmasstransfer.2015.06.007
0017-9310/

which different processes will take place [11]. It is important to highlight that other applications within the mining industry that do not necessarily include the use of gases such as the case of solvent extraction could also benefit from the scheme presented here because the droplet sizes will define the rate at which the aqueous and organic phases separate in the settlers [12].

In general, bubble characterization methods could be based on passive acoustic detection, capillary suction probes, high-speed photography, endoscopic optical probes and optical waveguide sensors [13]. Lin et al. [14] used three parallel planes of laser light between two photo detectors to measure the refractive index, size and velocity of the bubbles. The detectors record multiple refracted (and reflected) beams to estimate the parameters as the bubbles pass through. Kawaguchi et al. [15] presented an interferometer laser imaging technique to size bubbles and droplets. They used image analysis to estimate diameters as low as approximately 200 μm. Leung et al. [16] proposed a real-time bubble monitoring approach and used five different carbonated drinks to flow through a channel network passing through a laser beam. Position-sensitive detectors measured the displacement of the laser beam due to the lower refractive index when a bubble passed.

Vazquez et al. [13] estimated the size of air bubbles by using photographic, acoustic, and an inverted funnel or the capillary suction probe based techniques. The authors reported that the inverted funnel based technique gave a 0.5% repeatability error with a 50-bubble set, while the photographic method gave an accuracy between 86% and 99% with a 5% repeatability error. The passive acoustic method provided an accuracy of 97% and 99% with a repeatability of 0.3%. It was concluded that the acoustic method provided accurate estimation together with the optical based scheme. Performance of the optical method was limited by the lighting conditions and required the purity of the fluid medium.

The majority of the acoustic based techniques rely on the ability of the bubble to oscillate with a resonance frequency that is approximately inversely proportional to its radius. The use of a single excitation frequency has been shown to have limitations, such as the masking of small bubbles in the presence of large ones, thus compelling researchers to employ two frequencies to exploit the nonlinearity associated with the high amplitude pulsations. The nonlinear mixing of signals, when using two frequencies, may reduce the probability of false triggering and provide a relatively accurate method to detect and size gas bubbles [17]. Pulsed ultrasound has also been employed for studying decompression sickness. When humans and animals return from pressurized environments, bubbles inside the blood evolve from their tissue fluids [18–20]. It is worth highlighting that most of the bubble resonance frequency based methods generally consider a simplistic model and ignore the effects related to the elastic properties of bubble walls, stiffness, multi-bubble effects, inertia, and the proximity of the boundaries [21].

Duraiswami et al. [22] used a dispersion relation for the propagation of sound waves in bubbly liquids for bubble counting. Bubbles were artificially generated in the experiments to estimate the bubble population. The authors also developed a technique to measure the bubble size distributions using photography and reported that the bubble distributions obtained by both methods were consistent. Wu and Chahine [23] developed a device, termed the "Acoustic Bubble Spectrometer", to estimate bubble size distribution by measuring frequency-dependent attenuations and phase velocities of the sound waves. Furthermore, in the boiling process, the effects of the electrical field of the bubbles are reported in [24]. The bubble shape and ebullition cycle can be modified by strong electric fields. Furthermore, by using the volume of fluid method (VOF), the interaction of the electric field with the hydrodynamics in two fluid systems has been investigated in [25] to capture the motion of drops under the di-electrophoretic effect.

In this paper, we propose a new technique to discriminate between different bubble sizes utilizing only a single sensor and signal processing techniques. The discrimination is based on the Euclidean distance between templates of the different size classes computed using the short-time Fourier transform. The strategy was applied to data obtained using 3D computational fluid dynamics (CFD) simulations. The results presented here suggest that the proposed technique can lead to the discrimination of bubble sizes with a single sensor point by using signal processing methods. Furthermore, the model proposed in this paper indicates that the analysis window size may play a significant role in the discriminability depending on the range of target bubble sizes. Finally, the scheme described here is interesting from a theoretical and application viewpoint.

2. Computational fluid dynamics simulations

For multiphase fluid dynamics in the volume of fluid (VOF) formulation, the fluids are not interpenetrating. For each phase, the volume fraction of the phase is introduced in each computational cell, so that the volume fractions of all phases sum to unity. The fields for all variables and properties are shared by the phases and represent volume averaged values as long as the volume fraction of each of the phases is known at each location. Thus, the variables and properties in any given cell are either purely representative of one of the phases or representative of a mixture of the phases, depending upon the volume fraction values [26].

The VOF model uses the continuity and momentum equations for incompressible fluids to describe the fluid dynamics of both the gas and liquid phases:

$$\vec{\nabla}\cdot\vec{u}=0 \tag{1}$$

$$\frac{\partial\rho\vec{u}}{\partial t}+\vec{\nabla}\cdot\rho\vec{u}\cdot\vec{u}=-\vec{\nabla}p+\mu_{eff}\nabla^2\vec{u}+\rho\vec{g} \tag{2}$$

where u is the velocity and p is the pressure. The density ρ and effective viscosity μ_{eff} of the fluid are given by:

$$\rho(\vec{x},t)=F(\vec{x},t)\rho_l+[1-F(\vec{x},t)]\cdot\rho_g \tag{3}$$

$$\mu_{eff}(\vec{x},t)=F(\vec{x},t)\mu_{l,eff}+[1-F(\vec{x},t)]\cdot\mu_{g,eff} \tag{4}$$

where F is the local volume fraction of the fluid. Its value is one in the liquid phase and zero in the gas phase. A value between one and zero indicates a density interface. The subscripts l and g indicate the liquid and gas phases, respectively. The force due to the surface tension acting on the gas liquid interface was considered in the present formulation using the water surface tension and a contact angle with the wall. The model solves the scalar advection equation for the quantity F; this equation states that F moves with the fluid:

$$\frac{\partial F}{\partial t}+\vec{u}\cdot\vec{\nabla}F=0 \tag{5}$$

For air, we have set a density $\rho_g = 1.225$ [kg/m^3] and a viscosity $\mu_g = 1.79\times10^{-5}$ [kg/ms]. For the water, we used a density $\rho_l = 1000$ [kg/m^3] and a viscosity $\mu_l = 0.001$ [kg/ms]. The surface tension was set as $\sigma = 0.0728$ [N/m], the gravity acceleration was set as 9.81 [m/s^2], and the contact angle of water was set as 60^0. The geometry model is a cylindrical vessel with a radius of 20 mm, and it is filled with 40 mm of water. The height of the vessel is 50 mm. Air is injected in the bottom with a tube with a radius of 1 mm, and the injection tube length is 5 mm. We have injected air at four different velocities, namely, 0.02, 0.05, 0.2 and 0.4 m/s.

2.1. Numerical method

The VOF model was solved using the commercial solver Fluent 6.3.26 on 64-bits. This package is a finite volume solver that uses

body-fitted computational grids. Fluent uses a co-located scheme, whereby pressure and velocity are both stored at the cell centers [27]. The pressure–velocity coupling is obtained using the SIMPLEC algorithm. We use the geometrical reconstruction scheme to obtain the face fluxes, when the cell is near the interface between two phases [26]. For the time dependent calculations, we use a first-order implicit time scheme with convergence criteria of 0.001. The algorithm used for pressure was body force weighted and for the momentum, the power law scheme was used [27].

The time step was chosen so that in each time step, the convergence criterion of the residuals of continuity and momentum of 0.001 was reached. We set a maximum of 20 iterations in each time step. For the cases with inlet velocities of 0.02 and 0.04 m/s, the time step was 8×10^{-6} s, and for the cases with inlet velocities 0.2 and 0.4 m/s, the time step was 2×10^{-6} s.

We used a 3D grid with 521,601 cells for the simulations. We used tetrahedral elements, and the grid was refined at the air inlet. The velocity magnitude in [m/s] and static pressure in [Pa] at the control point were obtained with a numerical sensor, making a vertex averaged value in the position of 10-mm high at the centerline of the cylindrical vessel. The velocity and pressure magnitude at this point were recorded as the data for the signal processing analysis.

The workstation used to perform the simulations in this work is based on Xeon E5620 with eight processors that have a 2.4-GHz clock speed, 24 GB RAM memory, with 64 bits and running on the Linux Debian 6.0 operating system. The simulation time for the case of 0.05 [m/s] inlet velocity based on 1.8 s employing 8×10^{-6} time steps was approximately 6 days of CPU time.

A CFD simulation in an axisymmetric vessel with the same methodology was reported in [28]; however, the 2D restriction made the bubble size and frequency not completely realistic.

2.2. Preliminary theoretical analysis of the hydrodynamics

The bubble size and bubble velocity have been studied using dimensionless numbers. Table 1 presents relevant dimensionless numbers commonly used to characterize gas dispersion in gas–liquid systems.

It has been reported that the bubble terminal velocity is related to the bubble size and bubble shape [29]. In general terms, at smaller bubble sizes (below 1 mm in diameter with an Eotvos number below 0.15), the bubble shape is close to a perfect sphere and the terminal velocity increases with the bubble size. Above a 1-mm bubble diameter, the terminal velocity reaches a narrow region (roughly between 10 and 40 cm/s or Eotvos numbers between 0.15 and 40.0) where upper values are reached in pure water conditions while lower values are a function of the water contamination indicating that the latter reduces the bubble velocities. This intermediate region is characterized by bubbles with ellipsoidal shapes, bubble boundary oscillations and Reynolds numbers between 450 and 4700. Above 20-mm bubble diameters (Eotvos numbers above 40), the bubble terminal velocities increase with the diameter, exhibiting spherical cap shapes.

From Table 1, it can be observed that in the search for variables that may impact the rate of gas–liquid reactions, bubble size and bubble velocity have received special attention. There are a set of mathematical relationships between bubble size, bubble velocity and bubble shape. The bubble volume V_B has been associated with the air flow rate q crossing a closed round section [30].

$$V_B = \frac{\pi d_b^3}{6} = 1.378 q^{6/5} g^{-3/5} \tag{6}$$

Other research studies have estimated the Reynolds number using the following mathematical expression [31]:

$$Re = \left[\left(\frac{4/3 Eo^{1.5} Mo^{-0.5}}{24} \right)^{-1.2} + \left(\frac{4/3 Eo^{1.5} Mo^{-0.5}}{0.43} \right)^{-0.6} \right]^{-0.83} \tag{7}$$

Table 2 presents a summary of the conditions tested in the CFD computations. These outcomes will be compared to the signal analysis. The Takadi number indicates that cases 1 and 2 exhibit the formation of spherical bubbles, while cases 3 and 4 exhibit spheroidal bubble shapes [32,33]. The Weber number indicates that for cases 1 and 2, the stability of spherical bubbles is high and no split should be produced. The critical Weber number above in which bubbles split has been reported in a range between 1.4 and 4.7 [34]. The latter indicates that the conditions in case 4 would promote bubble split. Case 3 is an intermediate situation that needs further analysis. Fig. 1 shows the snapshot of the four bubble size classes obtained by CFD i.e., (a) 0.02 m/s, (b) 0.05 m/s, (c) 0.2 m/s, and (d) 0.4 m/s. As expected, it can be observed that the bubble size increases when increasing the gas flow rate and, at the same time, the bubble shape is increasingly distorted.

3. Signal processing analysis and discrimination

3.1. Filtering and down sampling

Because the signals were produced at a very high sampling rate (equal to the time step), they are first down sampled (or decimated). The down sampling is performed to bring the signals within a reasonable working range and so that they have the same sampling rate. Down sampling is also necessary because the bandwidth of the frequency spectrum is proportional to the sample rate. This means that if the signal is sampled at a rate Fs, the spectrum will have a frequency range from zero to Fs/2. The decimation process includes low-pass filtering for the signals to mitigate distortion due to aliasing. An eighth-order Chebyshev Type I low-pass filter with a cut-off frequency of $8 \times \frac{Fs/2}{R}$, where R is the down sampling factor, was used.

3.2. Frequency domain analysis based on discrete Fourier transform

Analyzing the observed signals in the time domain may not effectively reveal sufficient information to discriminate the

Table 1
Dimensionless numbers commonly evaluated in gas-dispersed aqueous solution to characterize these systems.

Dimensionless numbers	Equation
Morton	$Mo = \frac{g\mu_l^4}{\rho_L \sigma^3}$
Eotvos	$Eo = \frac{g\rho_L d_b^2}{\sigma}$
Reynolds	$Re = \frac{\rho_L u_b d_b}{\mu_L}$
Tadaki	$Ta = ReMo^{0.23}$
Weber	$We = \frac{\rho_L u_b^2 d_b}{\sigma}$
Froude	$Fr = \frac{u_b}{(gd_b)^{0.5}}$

Table 2
Summary of the preliminary analysis of the bubbly flow.

Case	u_{air} [m/s]	d_b [mm]	$Mo \times 10^{-11}$	Eo	Re	Ta	We	u_{bt} [m/s]
1	0.02	1.15	2.54	0.18	215	0.8	0.01	0.19
2	0.05	1.66	2.54	0.37	379	1.4	0.06	0.23
3	0.20	2.89	2.54	1.13	761	2.8	1.58	0.26
4	0.40	3.81	2.54	1.96	1011	3.7	8.35	0.26

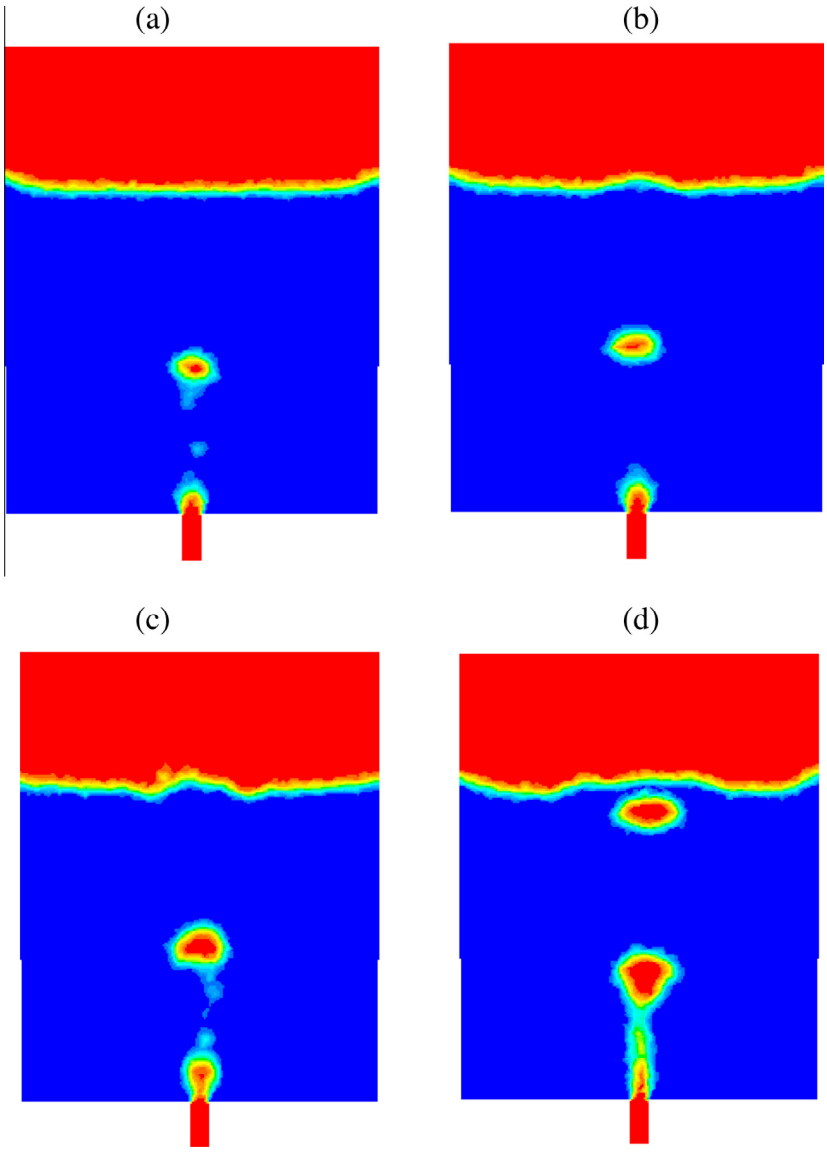

Fig. 1. The four bubble size classes obtained by CFD, i.e., (a) 0.02 m/s, (b) 0.05 m/s, (c) 0.2 m/s, and (d) 0.4 m/s.

different bubble size classes. For instance, cross-correlation potentially has the following limitations in pattern recognition or classification tasks with time varying signals: it is not suitable for short-term frame based pattern classification because it requires evaluation at all possible lags between reference and testing windows; hence, it is constrained by the short-term analysis windows, it restricts the analysis to the time domain, and the use of model-based classification is not straightforward. The signals are therefore transformed into the frequency domain because this allows us to see how the energy of the signal is distributed over a range of frequencies. The signals can be converted to the frequency domain, for example, using the discrete Fourier transform (DFT), obtained through Eq. (8) to provide the spectrum of the signals. The DFT computations assume the signal is periodic i.e., it has an integer number of complete cycles, and determine its frequency contents. A fast Fourier transform is used to implement the DFT that significantly reduces the computational complexity. If $f(n)$ is the discrete time signal, where n is the discrete time index, i.e., $n = 1, 2, \ldots, N$, the DFT can be computed as

$$F(\omega) = \sum_{n=1}^{N} f(n) \cdot e^{-\frac{j2\pi\omega n}{N}}, \quad \omega = 1, 2, \ldots, K \tag{8}$$

where $F(\omega)$ is the DFT coefficient at the ωth frequency bin and K is the total number of frequency bins. It is worth highlighting that in the current paper, we are proposing a framework where we are able to discriminate between different bubble sizes with only one sensor. In this context, the Fourier transform provides a suitable framework, and a specific comparison with other transforms (i.e., discrete cosine, wavelet, etc.) lies outside the scope of this article.

3.3. Short-time Fourier transform

While the DFT of the entire time domain signal contains information regarding the spectral components within the signal, it cannot detect how the different frequencies change over time. So, the time–frequency analysis is performed using the windowed or short-time Fourier transform (STFT). The window, for example, a Hamming window, is translated across time typically with an overlap of 50% between adjoining windows. The STFT is mathematically expressed as

$$F(t, \omega) = \sum_{n=1}^{N} f(t+n).w(n).e^{-\frac{j2\pi\omega n}{N}}, \quad \omega = 1, 2, \ldots, K \tag{9}$$

Table 3
Classifying bubble sizes by template matching based on Euclidean distances.

	TEMPLATE			
	Class 1 (C1)	Class 2 (C2)	...	Class C (CC)
INPUT (I) feature vector	$E_{dist}(\mathbf{I},\mathbf{C1})$	$E_{dist}(\mathbf{I},\mathbf{C2})$	...	$E_{dist}(\mathbf{I},\mathbf{CC})$

where t and ω are the time and frequency indices, respectively, while $w(n)$ is the window function, commonly a Hamming window, given as

$$w(n) = 0.54 - 0.46 * cos\left(\frac{2\pi n}{N}\right). \tag{10}$$

Eq. (9) gives the time–frequency representation of the signal i.e., how the signal's energy is distributed at different frequencies over time. The spectrogram can be obtained by taking the magnitude squared as $O(t,\omega) = |F(t,\omega)|^2$.

A template or feature vector is then obtained by taking the mean of the spectrogram across the time dimension. This method is advantageous in that the average values are analyzed, and also a comparison between signals could still be made even if they are of a different time duration.

$$Template = P(\omega) = \frac{\sum_{t=1}^{T} O(t,\omega)}{T} \tag{11}$$

where T is the total number of windows in a template.

3.4. A discussion on the length and number of analysis windows

Before proceeding to the description on how the template defined in Eq. (11) is used to discriminate among different bubble sizes based on Euclidean distance based template-matching, it is deemed necessary to provide insight on how the length of the STFT analysis window, N, and the total number of windows in the template, T, may potentially influence the discrimination performance. The template defined in Eq. (11) corresponds to a subset of T windows extracted from the whole signal. According to (11), each template requires the information of T windows, where each window is composed of N samples. The STFT analysis window size determines the resolution of the spectral analysis: the wider the window, the higher the spectral resolution. Additionally, the time interval covered by each template, i.e., $T \times N$, conditions the time resolution: if $T \times N$ is small, the dynamics of the process (i.e., bubble size and bubble rate) is better represented. According to traditional signal processing theory, for a reliable and accurate spectral analysis, the STFT analysis window length should be such that it captures several bubble events. Adopting this strategy in the case of the smaller bubbles that have a relatively lower bubble rate would thus require the use of a very large STFT window size, which in turn could potentially impose limitations on how to describe the temporal variations contained in the signals. However, we show that if the analysis window is short enough, i.e., the time signal within it can be approximated as a straight line, the signal represented by the template can be modeled as a piecewise linear function. Under this condition, the window analysis is sufficient to preserve the information related to the average of the signal and of the absolute value of the signal slope. By employing the piecewise linear approximation, the signal corresponding to a given template can be expressed as:

$$f(t) = \{a_i t + b_i . \because t_i \leqslant t < t_{i+1}, \quad \text{where } 1 \leqslant i \leqslant T \tag{12}$$

where each STFT analysis window i can be expressed as

$$f_i(t) = \begin{cases} a_i t + b_i \ for \ t_i \leqslant t < t_{i+1} \\ 0, \ \text{elsewhere} \end{cases}$$

where t_i and t_{i+1} define the time interval of the ith window. Note that the model shown here corresponds to the continuous time domain, while in the following sections for the ease of implementation, the discrete version is used. Let $F_i(\omega)$ be the Fourier transform of the ith window $f_i(t)$, while $\mathcal{F}$ is the Fourier operator.

$$F_i(\omega) = \mathcal{F}\{f_i(t)\} = \mathcal{F}\{a_i t\} + \mathcal{F}\{b_i\}, t_i \leqslant t < t_{i+1}$$

The template is defined as the average Fourier transform of all of the analysis windows within the template. For the rectangular window case, the template can be written as:

$$P(\omega) = \frac{1}{T}\sum_i |\mathcal{F}\{f_i(t)\}|^2 \tag{13}$$

where the continuous time Fourier transform is defined as:

$$\mathcal{F}(f_i(t)) = \int_{-\infty}^{\infty} f_i(t).e^{-j\omega t} dt$$

$$\mathcal{F}(f_i(t)) = \int_{-\infty}^{\infty} a_i t.rect\left(\frac{t-t_0}{\delta}\right) \cdot e^{-j\omega t} dt + \int_{-\infty}^{\infty} b_i \cdot rect\left(\frac{t-t_0}{\delta}\right).e^{-j\omega t} dt \tag{14}$$

where $\delta = t_{i+1} - t_i$ and $t_0 = \frac{t_{i+1}+t_i}{2}$.

By replacing the Fourier transform according to Eq. (14) in Eq. (13), the template $P(\omega)$ is expressed as:

$$P(\omega) = \frac{1}{T}\sum_i \left| a_i \left(\frac{e^{-j\omega t_{i+1}}}{(-j\omega)^2}[-j\omega t_{i+1} - 1]\right) - a_i \left(\frac{e^{-j\omega t_i}}{(-j\omega)^2}[-j\omega t_i - 1]\right) + b_i \cdot Sa\left(\frac{\omega\tau}{2}\right) \cdot e^{-j\omega t_0} \right|^2 \tag{15}$$

As seen in Eq. (15), the absolute value of the slope of each segment a_i is preserved. The average value of $f(t)$ that corresponds to the Fourier transform evaluated at $\omega = 0$ can be estimated from:

$$\overline{f(t)} = \frac{1}{T}\sum_{i=1}^{T} \overline{f_i(t)}$$

where

$$\overline{f_i(t)} = \frac{1}{t_{i+1} - t_i}\int_{t_i}^{t_{i+1}} (a_i t + b_i) dt = \left[\frac{a_i}{2} \cdot [t_{i+1} + t_i] + b_i\right] \tag{16}$$

According to (15) and (16), a short analysis window can be a substitute for a traditional window size that covers several bubble events

Table 4
The inter/intra-class distance matrix used for classification performance evaluation.

	Target template			
	Class 1	Class 2	...	Class C
Ref template				
Class 1	E_{dist} (Class1ref, Class1target)	E_{dist} (Class1ref,Class2 target)	...	.
Class 2	E_{dist} (Class2ref,Class1target)	E_{dist} (Class2ref,Class2 target)		.
⋮	⋮	⋮	⋮	
Class C	E_{dist} (ClassCref,Class1target)	E_{dist} (ClassCref,Class2 target)	...	.

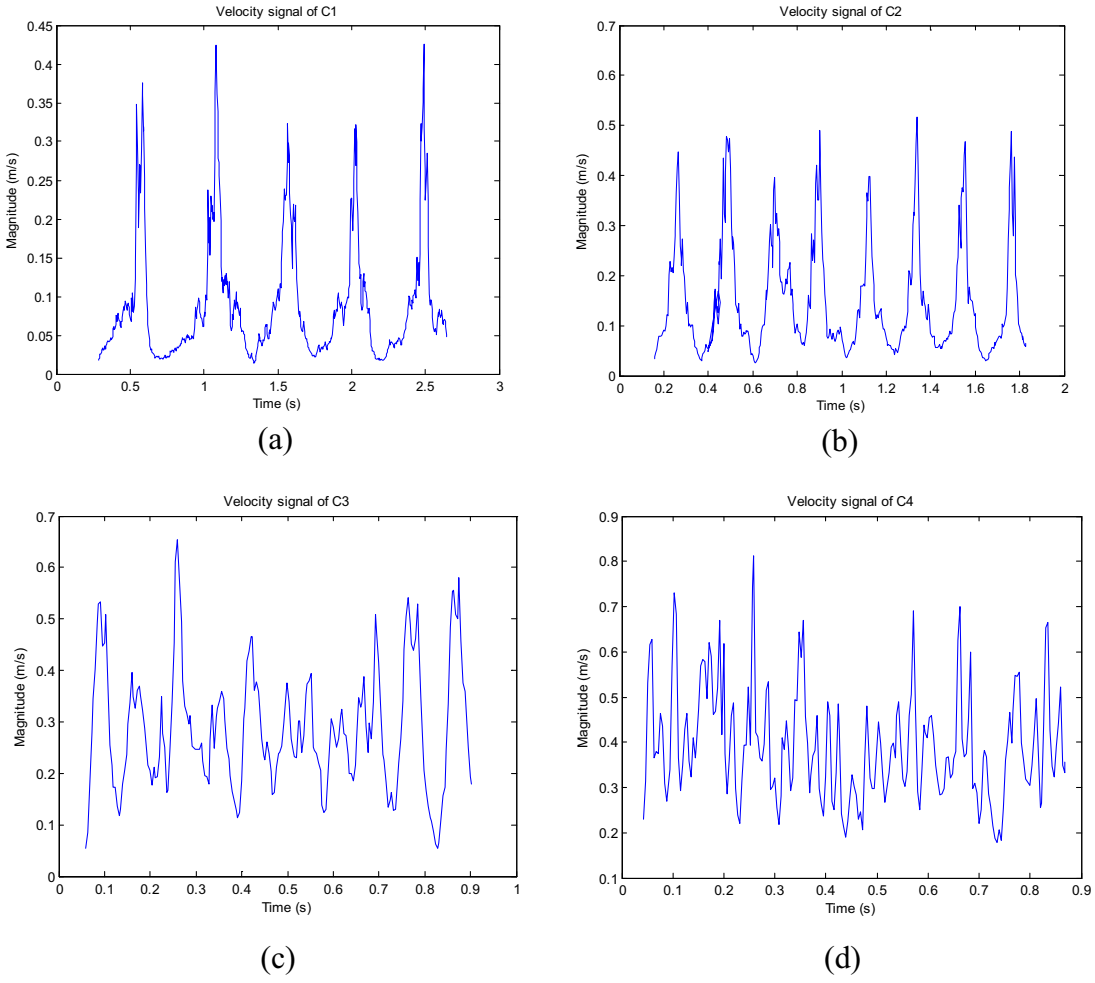

Fig. 2. Time domain velocity signals of the four different size classes.

if only the averages of the signal and the absolute values of the signal slopes need to be preserved. Once the analysis window size is defined, T in Eq. (11) should be determined. If a short analysis window is selected, T should be high enough to reliably represent the process features (i.e., signal average and slope) and should be lower than the temporal resolution that is required. If a larger analysis window is adopted (i.e., several bubble events per window), T would be limited by the temporal resolution required.

3.5. Euclidean distance based template matching: nearest neighbor classification

Signals are classified into their respective size class based on their Euclidean distance (E_{dist}) from the templates of known classes. This means that Euclidean distances are first calculated for the input signal's feature vector (template) with all of the available templates of different size classes as shown in Table 3, and the class giving the smallest distance (or the nearest neighbor) is the resulting size class. Let $\boldsymbol{I} = i_1 + i_2 + \ldots + i_y$ and $\boldsymbol{E} = e_1 + e_2 + \ldots + e_z$ be the feature vectors or templates of two signal classes. Thus, the Euclidean distance between vectors $\boldsymbol{I}$ and $\boldsymbol{E}$ can be calculated as:

$$E_{dist}(\boldsymbol{I}, \boldsymbol{E}) = \sqrt{(i_1 - e_1)^2 + (i_2 - e_2)^2 + \ldots + (i_y - e_z)^2} \quad (17)$$

The input signal feature vector is classified according to the minimum Euclidean distance criterion

$$\textit{Input signal class} = \; argmin_{C_i}\{E_{dist}(I, C_i)\} \quad (18)$$

where $C_i = [C_1, C_2, \ldots, C_{Nc}]$, and Nc is the number of classes of bubble sizes.

3.6. Discrimination performance evaluation

To evaluate the performance of the method described above, a matrix is constructed by computing the Euclidean distances between the reference feature vectors and the target templates as shown in Table 4. For the performance evaluation, both the reference and target classes are assumed to be known a priori. The first 50% of the data is used as reference class and the second 50% as target class. The order of selecting the reference and target could be reversed *i.e.*, the second half could be used as the reference and the first half as the target. After computing the Euclidean distances, the inter/intra-class matrix is formed as follows.

Once the inter/intra-class distance based matrix is formed, a confusion versus score is calculated to determine the level of discrimination as

$$\textit{Confusion score} = \textit{mean of diagonal values} / \textit{mean of non-diagonal values}$$

Theoretically, the values on the principal diagonal should be very small, and the values on the off diagonal should be relatively very large. If this is the case, then it indicates that the discrimination is

good and the confusion score is low. A higher score would indicate confusion in discrimination.

4. Results and Discussion

Air was injected with four different initial velocities yielding four different bubble size classes, i.e., 0.02, 0.05, 0.2, and 0.4 m/s, hereafter referred to as C1, C2, C3 and C4, respectively. Velocity and pressure signals from a single sensor located 10 mm from the bottom of the vessel were analyzed. The magnitude of the velocity signals measured by the sensor is shown in Fig. 2, and the pressure signals are shown in Fig. 3. The signals from the different bubble sizes were down sampled so that they had the same sampling rate of 250 samples/s.

Using the simulation data, the rate of the bubbles was estimated for each size class by using the average duration between the peaks in Fig. 2, indicating events crossing the sensor. From the estimated bubble rate (number of bubbles per second), the frequencies were calculated as 2.08, 4.69, 11.76, and 17.66 Hz for C1, C2, C3, and C4, respectively. It is possible to extract directly from the time domain pressure and velocity results the main frequency of bubble generation. It was found that the linear gas velocities increase with the frequency, which is in agreement with past research works published [35] (see Fig. 2).

Fig. 4 depicts the time–frequency (spectrogram) representation of the velocity signals shown in Fig. 2. The spectrograms show how the energy in distributed in different frequencies over the duration of the signals.

The discriminability between the four size classes for the observed velocity and pressure signals is analyzed by constructing the inter/intra-class Euclidean distance based matrices, as described in Section 3.6. The matrices are obtained using an STFT analysis window of 8 and 64 samples for both the velocity and pressure signals. With the sampling rate of 250 samples/s, an STFT analysis window of 8 samples means a 32-ms segment of the signal in the time domain, while a STFT window of 64 samples is 256 ms. The matrices and their corresponding confusion scores for the velocity and pressure signals with a window size of eight samples are shown in Tables 5 and 6, respectively. The matrices are normalized with their corresponding maximum values.

It can be observed that the elements at the principal diagonal are considerably smaller compared to the non-diagonal elements of their corresponding rows and columns. This indicates that the four classes are well discriminated, as also suggested by the low

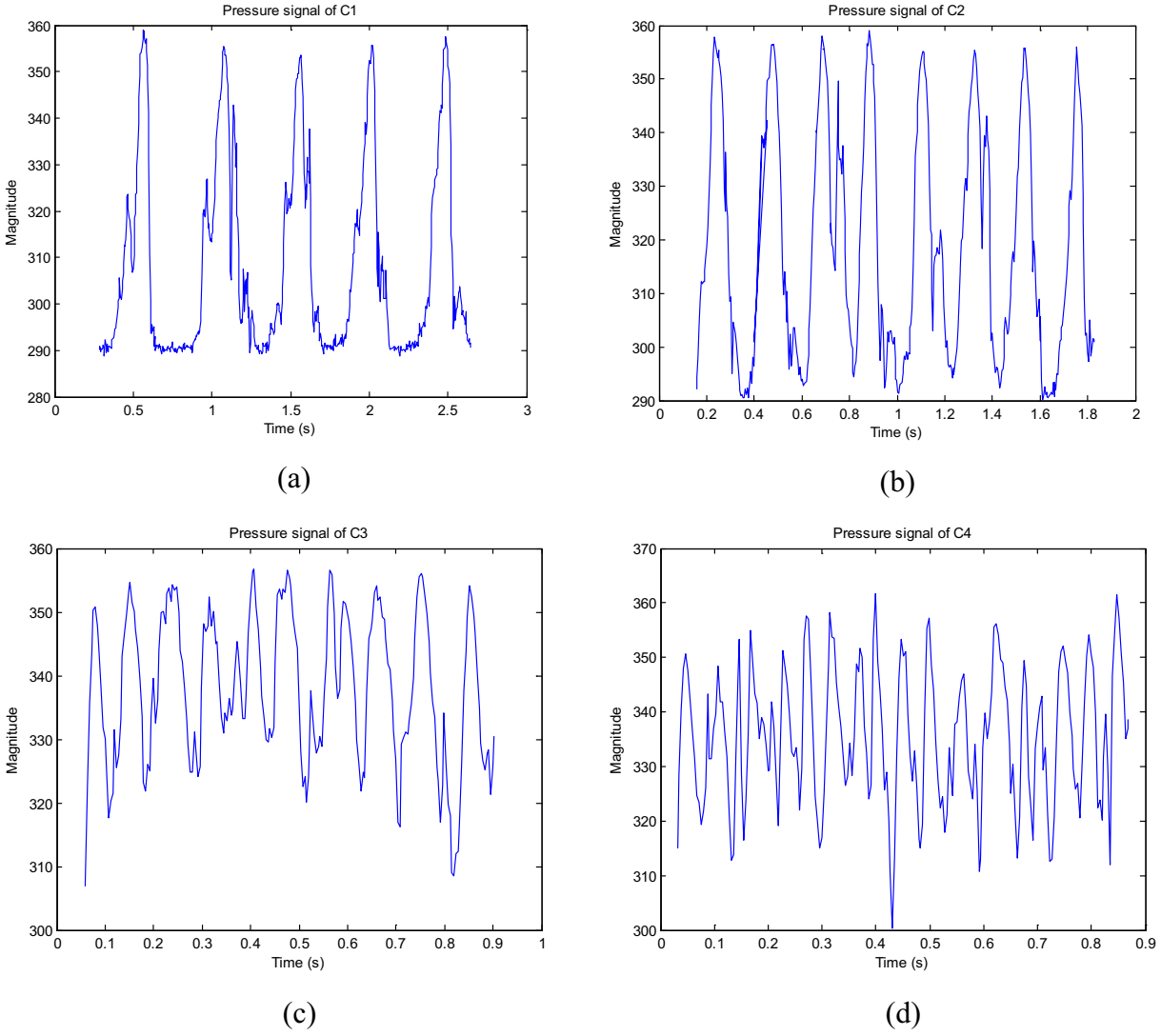

Fig. 3. Time domain pressure signals of the four different size classes.

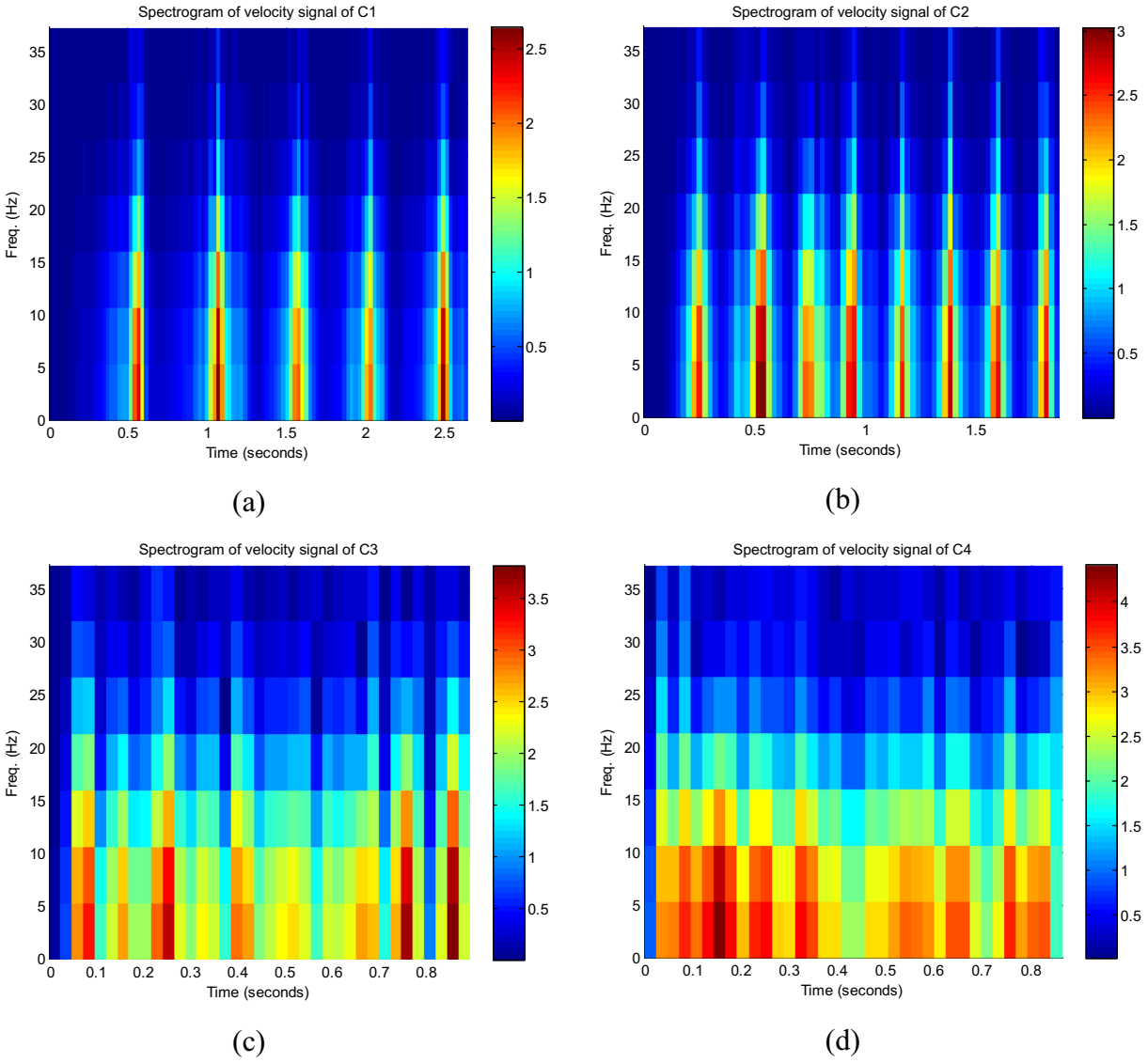

Fig. 4. Spectrograms of the velocity signals for the corresponding four different size classes shown in Fig. 2.

Table 5
Inter/intra-class distance matrix for velocity signal with STFT window of 8 samples.

VELOCITY SIGNAL (8 sample analysis window)					
Ref template	Target template				
		C1	C2	C3	C4
	C1	0.0163	0.1235	0.5177	0.8454
	C2	0.0901	0.0175	0.4113	0.7390
	C3	0.4624	0.3552	0.0391	0.3668
	C4	1.0000	0.8928	0.4987	0.1710
Confusion score = **0.1161**					

Table 6
Inter/intra-class distance matrix for pressure signal with STFT window of 8 samples.

PRESSURE SIGNAL (8 sample analysis window)					
Ref template	Target template				
		C1	C2	C3	C4
	C1	0.1414	0.3777	1.0000	0.9345
	C2	0.2321	0.0043	0.6265	0.5610
	C3	0.7537	0.5173	0.1050	0.0396
	C4	0.7571	0.5207	0.1016	0.0360
Confusion score = **0.1339**					

confusion score of 0.1161. The pressure signal also yields nearly similar results, giving a confusion score of 0.1339.

Tables 7 and 8 provide the inter/intra-class distances for the STFT with an analysis window of 64 samples. The results for the STFT analysis window size of 64 samples also provide discrimination between the different classes. However, there is a slight degradation in the discrimination performance compared to that with the STFT window of eight samples, as indicated by the increased score value of 0.1894 for the velocity signal and 0.1408 for the

Table 7
Inter/intra-class distance matrix for velocity signal with STFT window of 64 samples.

VELOCITY SIGNAL (64 sample analysis window)					
Ref template	Target template				
		C1	C2	C3	C4
	C1	0.0174	0.0588	0.3961	0.7493
	C2	0.0718	0.0306	0.3111	0.6630
	C3	0.4185	0.3771	0.0594	0.3183
	C4	1.0000	0.9589	0.6216	0.2678
Confusion score = **0.1894**					

Table 8
Inter/intra-class distance matrix for pressure signal with STFT window of 64 samples.

PRESSURE SIGNAL (64 sample analysis window)					
Ref template	Target template				
		C1	C2	C3	C4
	C1	0.1385	0.3039	1.0000	0.8421
	C2	0.2244	0.0620	0.6385	0.4818
	C3	0.8018	0.6356	0.0633	0.1049
	C4	0.7398	0.5730	0.1232	0.0398
Confusion score = **0.1408**					

Table 9
Distance for velocity signal with mean removed and STFT window of 8 samples.

VELOCITY SIGNAL, MEAN REMOVED (8 sample analysis window)				
	Target Template			
	C1	C2	C3	C4
Ref template				
C1	0.0535	0.4054	0.5282	0.2658
C2	0.4923	0.0624	0.1642	0.5491
C3	1.0000	0.5422	0.4304	0.9922
C4	0.9376	0.5122	0.3797	0.8683
Confusion score = **0.6269**				

Table 10
Confusion scores with and without the mean value removed from signals.

	Confusion scores			
	Velocity (8 sample)	Pressure (8 sample)	Velocity (64 sample)	Pressure (64 sample)
With mean	0.1161	0.1339	0.1894	0.1408
Without mean	0.6269	0.3562	0.5716	0.2810

pressure signal. Because the selection of the STFT analysis window size is the trade-off between time and frequency resolutions i.e., a smaller window gives poor frequency resolution and better time resolution, while a larger window provides better frequency and poor time resolution. The results suggest that when a window of eight samples is used and provides a better time resolution, information related to the bubble rate is captured and enhances the discrimination between the different size classes. However, when the analysis window size is increased to 64 samples where the time resolution is relatively poor and frequency resolution is better, the crucial information of the bubble rate is not fully captured and the discrimination performance deteriorates.

The rate of the bubbles, i.e., the number of bubbles per second, is related to the size of the bubbles. This means that because the larger bubbles are rising to the surface faster, they will have a higher bubble rate, i.e., more bubbles per second. A higher bubble rate also indicates a larger mean value of the signal, suggesting that the information regarding the bubble rate, and thus, the bubble size is embedded in the signal's mean value. To investigate if this is the case, the mean value is removed from the velocity and pressure signals and the inter/intra-class distance based matrices are reconstructed.

Table 9 shows the distance-based matrix for the velocity signal with the mean value subtracted and an STFT window size of eight samples. The results indicate that there is discrimination between the first two classes, while there is confusion between C3 and C4. Table 10 summarizes the confusion scores for the different STFT window sizes and signals with and without the mean value.

It can be observed from the results in Tables 10 that the discrimination performance deteriorates when the mean value is removed from the signals, suggesting that significant information for the different sizes is encoded in the time average or the rate of bubbles.

Fig. 5 depicts the confusion scores of the velocity signal by pairing the smaller sizes C1 and C2 and the larger sizes C3 and C4 for window sizes of 8 and 64 samples, as shown in Tables 5 and 7. Fig. 6 shows similar plots for the pressure signals by utilizing Tables 6 and 8. Both figures suggest that a smaller analysis window provides relatively better discrimination for smaller bubble sizes because the linear piecewise model approximates the signal better in these cases. Nevertheless, a larger analysis window can be used to provide a relatively uniform discrimination over a range of smaller and larger bubble sizes. This must be the result of the fact that the bubble size and bubble rate increases when the air mass flow also increases. Consequently, the bubble rate determines the average value of the signal: the higher the bubble rate, the higher the density of the bubble events and the higher the time average of

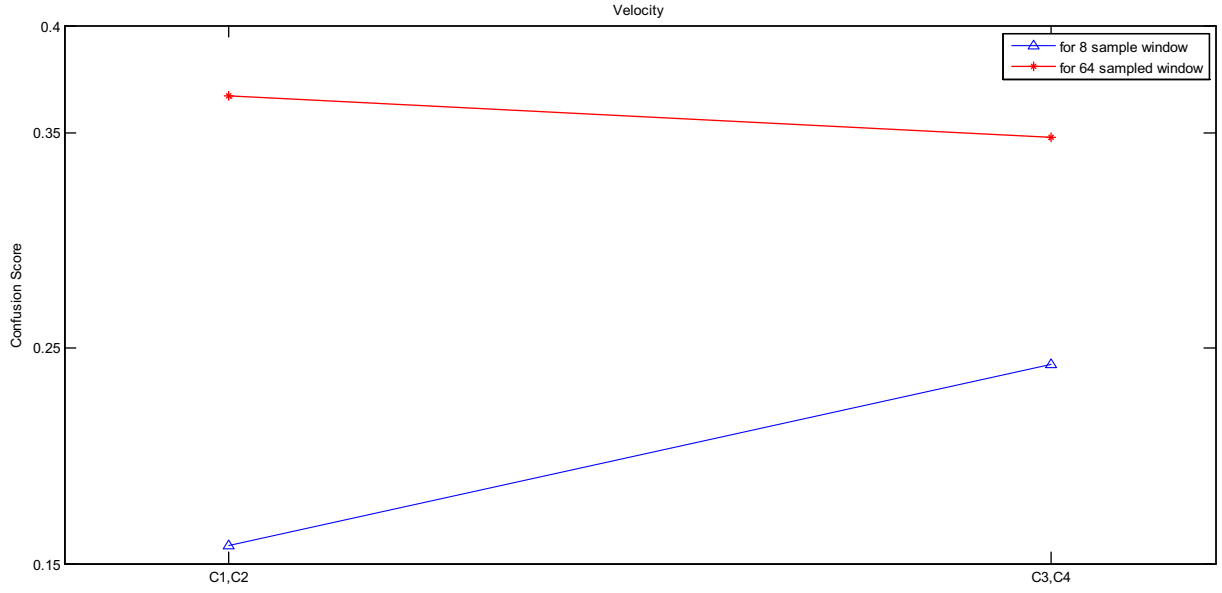

Fig. 5. Local confusion scores of paired size classes, [C1C2] and [C3C4], for velocity signal.

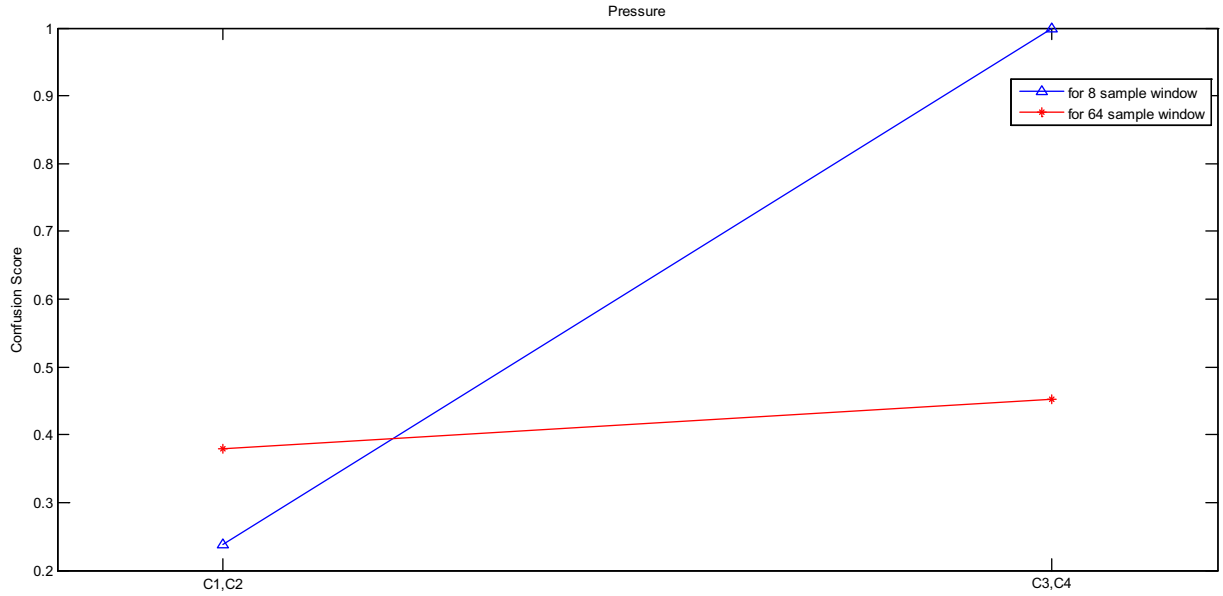

Fig. 6. Local confusion scores of paired size classes, [C1C2] and [C3C4], for pressure signal.

the signal are. Furthermore, the higher the bubble rate, the higher the average absolute value of the signal slope is. Both the mean value of the signal and the absolute signal slope are well preserved with a short analysis window when the piecewise function approximation discussed in Section 3.4 is applicable.

5. Conclusions

A new scheme to classify and determine the size of bubbles with a short-time Fourier transform based template representation is proposed and applied to data obtained by computational fluid dynamics simulations. The local pressure and velocity values from a single sensor are each analyzed by using signal processing methods. Fourier-based templates are estimated to represent the pressure and velocity signals. These templates are the result of short-term spectral analysis. The results presented here with a proposed inter/intra class distance based matrix analysis strongly suggest that these templates can be employed to discriminate bubble sizes by making use of a nearest neighbor pattern classification scheme. The mean of the signal and the absolute value of signal slopes were found to embed information regarding not only the bubble rate but also bubble sizes. The results presented here indicate that the proposed method is capable of discriminating among bubble sizes by using only one pressure or velocity sensor measurement. Moreover, the model presented in this paper suggests that the STFT analysis window size may play a significant role in the discriminability depending on the range of target bubble sizes. Finally, bubble size classification experiments with real data and the estimation of time-varying bubble size distributions are proposed for future research.

Conflict of interest

None declared.

Acknowledgment

This research is funded by the Chilean National Commission for Scientific and Technological Research (CONICYT), PIA, project ACT 1120.

References

[1] E.L. Paul, Handbook of industrial mixing: science and practice, in: Edwards L. Paul, Victor A. Atiemo-Obeng, Suzanne M. Kresta, p. cm. (Eds.), Sponsored by the North American Mixing Forum. Includes bibliographical references and index, (cloth: alk. Paper) John Wiley and Sons, Inc., Publication, 2003, 1353 p, ISBN 0-471-26919-0.
[2] A. Biesheuvel, L. van Wijngaarden, Two-phase flow equations for a dilute dispersion of gas bubbles in liquid, J. Fluid Mech. 148 (1984) 301–318.
[3] A.S. Sangani, A.K. Didwania, Dynamic simulations of flows of bubbly liquids at large Reynolds numbers, J. Fluid Mech. 250 (1993) 307–337.
[4] D.J. Nicklin, Two-phase bubble flow, Chem. Eng. Sci. 17 (1962) 693–702.
[5] D.W. Green, R.H. Perry, Perry's Chemical Engineers Handbook, 8th ed., McGraw-Hill Companies Inc., New York, Chicago, San Francisco, Lisbon, London, Madrid, Mexico City, Milan, New Delhi, San Juan, Seoul, Singapore, Sydney, Toronto, 2008.
[6] B. Lin, B. Recker, et al., Bubble size estimation for flotation processes, Miner. Eng. 21 (2008) 539–548.
[7] Y. Chun-hua, X. Can-hui, et al., Bubble size estimation using interfacial morphological information for mineral flotation process monitoring, Trans. Nonferrous Metals Soc. China 19 (2009) 694–699.
[8] R. Krishna, J. Ellenberger, Gas hold-up in bubble column operating in the churn-turbulent flow regime, AIChE J. 42 (9) (1996) 2627–2634.
[9] K.-D. Henkel, Reactor Types and Their Industrial Applications, Wiley-VCH Verlag GmbH & Co. KGaA, 2002. 968 p.
[10] J.B. Rubinstein, V.I. Melik-Gaikazyan, Characterisation of flotation froth, in: Janusz Laskowski, E.T. Woodburn (Eds.), Frothing in Flotation II: Recent Advances in Coal Processing, vol. 2, Gordon and Breach Science Pub, 1998 (Chapter 5).
[11] S.K. Ganguly, N. Varun, S. Kumar, P.K. Khatri, S.L. Jain, M.O. Garg, Laura A. Pellegrini, A review on gas–liquid reactions in light oil sweetening: kinetics and reactor design aspects, ChemBioEng Rev. 1 (5) (2014) 204–213.
[12] N.L. Eckert, L.S. Gormely, Phase separation in an experimental mixer-settler, Chem. Eng. Res. Des. 67 (1989) 175–184.
[13] A. Vazquez, R.M. Sanchez, E. Salinas-Rodriguez, A. Soria, R. Manasseh, A look at three measurement techniques for bubble size determination, Exp. Therm. Fluid Sci. 30 (2005) 49–57.
[14] S.M. Lin, D.R. Waterman, A.H. Lettington, Measurement of droplet velocity, size and refractive index using the pulse displacement technique, Meas. Sci. Technol. 11 (2000).
[15] T. Kawaguchi, Y. Akasaka, M. Maeda, Size measurements of droplets and bubbles by advanced interferometric laser imaging technique, Meas. Sci. Technol. 13 (2002) 308–316.
[16] S.A. Leung, J.B. Edel, R.C.R. Wootton, A.J. deMello, Continuous real-time bubble monitoring in microchannels using refractive index detection, Meas. Sci. Technol. 15 (2004) 290–296.
[17] T.G. Leighton, A.D. Phelps, D.G. Ramble, D.A. Sharpe, Comparison of the abilities of eight acoustic techniques to detect and size a single bubble, Ultrasonics 34 (6) (1996) 661–667.
[18] R.S. Mackay, G. Rubissow, Decompression studies using ultrasonic imaging of bubbles, IEEE Trans. Biomed. Eng. BME-25 (6) (1978) 537–544.
[19] E.O. Belcher, Quantification of bubbles formed in animals and man during decompression, IEEE Trans. Biomed. Eng. BME-27 (6) (1980) 330–338.

[20] A.A. Stravs, J. Wahl, U.V. Stockar, P.J. Reilly, Development of an ultrasonic pulse reflection method for measuring relative size distributions of air bubbles in aqueous solutions, Chem. Eng. Sci. 42 (7) (1987) 1677–1688.
[21] M.A. Ainslie, T.G. Leighton, Review of scattering and extinction cross-sections, damping factors, and resonance frequencies of a spherical gas bubble, J. Acoust. Soc. Am. 130 (2011) 3184–3208.
[22] R. Duraiswami, S. Prabhukumar, G.L. Chahine, Bubble counting using an inverse acoustic scattering method, J. Acoust. Soc. Am. 104 (5) (1998).
[23] X. Wu, G.L. Chahine, Development of an acoustic instrument for bubble size distribution measurement, J. Hydrodyn. Ser. B 22 Supplement 1 (5) (2010) 330–336.
[24] G. Tomar, G. Biswas, A. Sharma, S.W.J. Welch, Influence of electric field on saturated film boiling, Phys. Fluids 21 (2009) 032107-1–032107-8.
[25] G. Tomar, D. Gerlach, G. Biswas, N. Alleborn, A. Sharma, F. Durst, S.W.J. Welch, A. Delgado, Two-phase electrohydrodynamic simulations using a volume-of-fluid approach, J. Comput. Phys. 227 (2007) 1267–1285.
[26] E. Delnoij, J. Kuipers, W. Swaaij, Computational fluid dynamics applied to gas–liquid contractors, Chem. Eng. Sci. 52 (1997) 3623–3638.
[27] Fluent 6.3 User's guide, 2006.
[28] A. Valencia, M. Cordova, J. Ortega, Numerical simulation of gas bubbles formation at a submerged orifice in a liquid, Int. Commun. Heat Mass Transfer 29 (2002) 821–830.
[29] R. Clift, J.R. Grace, M.E. Weber, Bubbles, Drops and Particles, Academic Press, New York, 1978.
[30] J.F. Davison, B. Schuler, Bubble formation at an orifice in an inviscid liquid, Trans. Inst. Chem. Eng. 38 (1960). 335-242.
[31] C. Scheid, F. Puget, M. Halasz, G. Massarani, Fluid dynamics of bubbles in liquid, Braz. J. Chem. Eng. 16 (4) (1999) 351–358.
[32] T. Tadaki, S. Maeda, On the shape and velocity of single air bubbles rising in various liquids, Kagaku Kogaku 25 (1961) 254–264.
[33] J.R. Grace, Shapes and velocities of bubbles rising in infinite liquids, Trans. Inst. Chem. Eng. 51 (1973) 116–120.
[34] A.V. Nguyen, H.J. Schulze, Colloidal Science of Flotation, Marcel Dekker Inc., New York, Basel, 2003.
[35] M.C. Ruzicka, R. Bunganic, J. Drahos, Meniscus dynamics in bubble formation. Part I: Experiment, Chem. Eng. Res. Des. 87 (2009) 1349–1356.